Local Complementarity of Wind and Solar Energy Resources over Europe: An Assessment Study from a Meteorological Perspective

MARIO MARCELLO MIGLIETTA

National Research Council Institute of Atmospheric Sciences and Climate (ISAC-CNR), Lecce, and Joint Research Center, Institute for Energy and Transport, Ispra, Italy

THOMAS HULD AND FABIO MONFORTI-FERRARIO

Joint Research Center, Institute for Energy and Transport, Ispra, Italy

(Manuscript received 8 January 2016, in final form 30 August 2016)

ABSTRACT

To assess the possibility of a combined use of solar and wind energy over Europe, a continental-scale dataset, with high spatial and temporal resolution and covering three years of data (2012–14), is analyzed. The 100-m wind is taken from the ECMWF analyses/short-range forecasts. To obtain hourly values of potentially generated electricity, wind is transformed into normalized electricity-generation data by considering a normalized output function representing the most common wind turbines available in the European market. A strong monthly variation is present, showing the maximum potential at high latitudes in winter and shifting to specific areas in the Mediterranean Sea region in summer. Hourly data for solar radiation are extracted from the satellite-retrieval scheme of the Satellite Application Facility on Climate Monitoring (CM SAF). The energy output of photovoltaic systems is calculated by considering the amount of solar radiation that arrives at the surface of the photovoltaic modules. Together with the main functional dependence on latitude, the photovoltaic potential depends also on longitude, as a consequence of the average pressure patterns. Last, the local correlation of wind and solar resources is assessed. For hourly data, a weak anticorrelation prevails in the domain, suggesting a degree of local complementarity of the two sources in many regions. A strong effect from the diurnal cycle is observed in some regions. Also, a significant dependence on the month (higher absolute values in summer) and on the time scale (increase in absolute value with the extension of the time window that is considered for the correlation) is apparent.

1. Introduction

Solar irradiation and wind speed temporal dynamics are characterized by high natural temporal variability at time scales ranging from minutes/hours to seasons/years because of the dependence on weather and climate conditions (García-Bustamante et al. 2013). They exhibit different variability characteristics, however (Coker et al. 2013; Bett and Thornton 2016).

Their fluctuating nature represents a major issue for renewable energy production, since such variations may not match with the time distribution of the energy load demand on a continuous basis. Renewable energy sources as well the level of demand for electricity are extremely variable, changing on hourly, daily, and seasonal time scales as well as regionally. In this framework, the limited predictability of weather and climatic variability can significantly hinder effective grid management. Also, the intermittency of the two sources could lead to sudden electricity shortages, requiring the need for backup power systems. The spatial variability and temporal variability of the resources also influence the economic impact: an optimized renewable energy production system would need wind and solar electricity

production to complement each other as much as possible to minimize energy storage or to avoid curtailment. If the total available energy is relatively constant and predictable then the impact will be small, but if the energy production is highly variable and unpredictable then the impact may be large.

The complementarity of wind and solar resources is a key issue for overall energy generation (Gburčik et al. 2013). The independent use of these energy resources cannot provide a continuous power supply; therefore an optimally synchronized wind- and solar-based system should be implemented to provide more-even and less-fluctuating production (Santos-Alamillos et al. 2012; Monforti et al. 2014). Geographically dispersed wind (St. Martin et al. 2015) and photovoltaic (PV; Perez and Hoff 2013) generators are more likely to provide a smoother supply, as a consequence of the effect of random cancellation of fluctuations. Alternatively, hybrid solar–wind power generation systems that integrate the two energy resources can partially overcome this problem (Dos Anjos et al. 2015). This solution improves the efficiency of the system, improves the reliability of the energy supply, and reduces energy-storage requirements relative to systems that use a single source.

The combined use of solar radiation and wind for generating large amounts of electricity has to be carefully assessed to plan an increase in the exploitation of these two energy sources in the coming years. At the same time, the ideal share of the different renewables that guarantees a high efficiency remaining nearly constant in time (adjusted to the energy demand) should be identified, together with optimal location and spacing of energy plants. A comprehensive resource evaluation (Jerez et al. 2013a), also considering a climate change perspective (Jerez et al. 2015), should be pursued to achieve such goals.

The actual strategies on renewable energy production in Europe unfortunately suffer from being adapted to specific national requirements. As a consequence, the possibility for transnational cooperation is still limited at present, although the need for integration of national resources from different countries is growing.

A fundamental step toward a closer integration of renewable energy production among European countries would be the implementation of a high-resolution continental-scale wind and solar power database that is able to provide information on the average production from the two sources and on their temporal fluctuations. This information would allow one to quantify the need for balancing the renewable energy sources in terms of volume and time and would support the large-scale integration of wind and solar power, which is particularly important for the future European electricity network, which in turn will have to adjust to a growing number of sources of renewable energy.

The study that is presented here provides a contribution in this direction. To broadly assess the combined availability of wind and solar sources, this work analyzes a continental-scale wind and solar power dataset, with relatively high spatial and temporal resolution. Our study focuses on the general meteorological features that emerge from three complete years of data (2012–14). Because the current production of solar radiation and wind energy depends heavily on the variability of meteorological conditions, wind speed and solar radiation fields are here analyzed over Europe as a whole (whereas previous studies have focused mainly on a limited number of specific sites or areas). To identify the intensity and distribution of these two sources of energy and to consider their local complementarity in case of hybrid or nearby power plants, the anticorrelation of wind and solar resources is analyzed, allowing one to better tune the need for flexibility in energy-storage/backup systems. The complementarity between wind and solar power produced in different geographical areas, which is also an important aspect to be considered in planning strategic deployment of potential renewable energy production, is not considered in this study.

The paper is organized as follows. Section 2 describes the data used for the calculation of wind and photovoltaic energy. Section 3 provides a description of the wind energy potential in Europe over the three years considered, and section 4 analyzes the photovoltaic-potential data. Section 5 addresses the local complementarity of the two sources. Conclusions are drawn in section 6.

2. Data and method

Wind and solar power datasets are analyzed here at continental scale using high-temporal-resolution and high-spatial-resolution operational and climate-monitoring data. The purpose of this effort is to study the local complementarity of these two renewable energy sources in Europe. The time complementarity is evaluated here by means of correlation coefficients at different time scales (hourly, daily, and monthly) for a fixed point, supposing that the solar and wind plants are close to each other. The study is performed using data of solar radiation and wind speed that cover a period of three years (2012–14). The correlation is calculated only over the common geographical area of the two datasets, extending approximately from 30° to 60°N and from 15°W to 45°E. The exclusion of the northern part of the continent from the analysis is not relevant for the purposes of this study, considering that solar energy

production is relatively low at high latitudes and thus its contribution to the total energy is small for most of the year. On the other hand, the analysis includes the southern European countries, which have a stronger solar resource; in particular, the entire Mediterranean Sea Basin, considering also the African and Asian Mediterranean regions, is included. Both wind and solar irradiance data are analyzed by means of the Geographic Resources Analysis Support System (GRASS), an open-source geographical information system.

It is worth asking whether the selected years are representative of the long-term climate over Europe. Figure 1a shows the mean sea level pressure (MSLP) averaged over the 3-yr period analyzed here: the Azores high extends over the Iberian Peninsula, determining stable conditions in the region, while the central Mediterranean region is on average affected by a wide cyclonic circulation centered over the eastern Mediterranean; finally, a low pressure band extends to higher latitudes. The difference between the western and central Mediterranean is even more apparent when only the winter months (December–February) are considered, during which period a closed pressure minimum is centered over Italy (not shown).

Such configurations are consistent with the long-term climatological conditions (Kållberg et al. 2005), but the MSLP 3-yr anomaly in Fig. 1b suggests that an area extending from the British Isles to the Mediterranean region has pressure values that are on average slightly lower than normal in the period of 2012–14 while a positive anomaly is present from Greenland to Russia. This configuration is mainly of a consequence of the MSLP anomaly in the winter season, when values of ± 4 hPa, respectively, formed a dipole pattern. A similar feature, but more east–west oriented, can also be identified in the 500-hPa geopotential height anomaly, with anomalies up to ± 20 gpm, respectively, centered west of the British Isles and over eastern Europe (not shown). As a consequence, the wind speed was slightly more intense than normal in the Mediterranean area (up to about $1 \, \mathrm{m \, s^{-1}}$) while cloud coverage was slightly reduced (increased) relative to the average at high (low) latitudes (not shown).

a. Wind

The 100-m wind field, available from the European Centre for Medium-Range Weather Forecasts (ECMWF) analyses/forecasts since 2010, is used for the calculation of wind energy potential and variability. The new variable meets the need of calculating the wind speed at turbine height level and is the result of vertical linear interpolation from the two nearest ECMWF model levels, which are at approximately 70 and 110 m AGL. The new field represents a valuable improvement with respect to coarse reanalysis data and to direct extrapolation of ECMWF
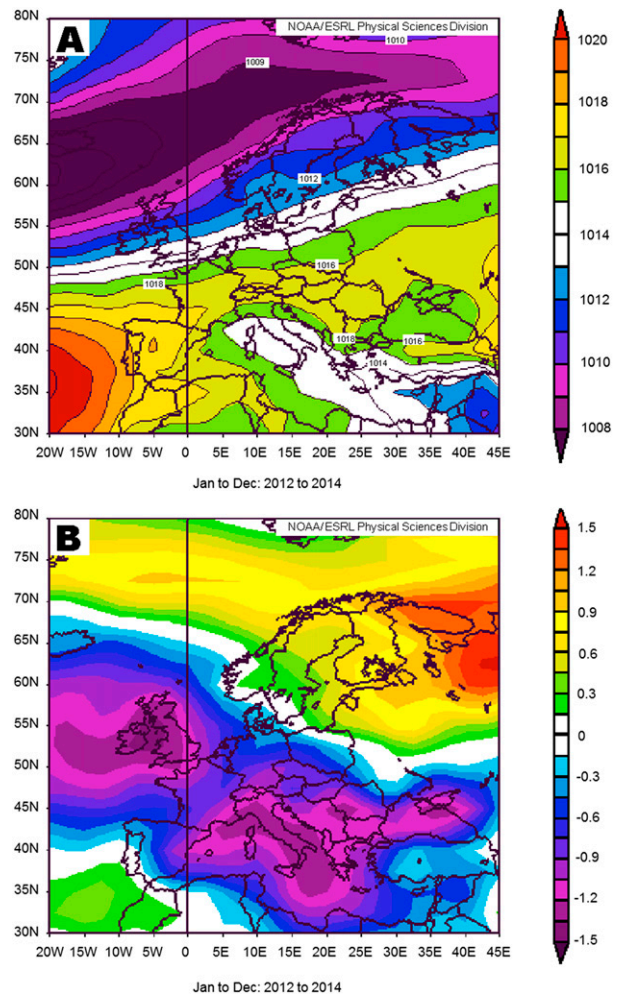

FIG. 1. (a) MSLP (hPa) averaged over the 3-yr period (2012–14), and (b) anomaly (hPa) with respect to the 30-yr climatological normal (1981–2010). Source: NCEP reanalysis, NOAA/Earth System Research Laboratory.

10-m wind, which was shown to produce a considerable degradation of energy power production with respect to observed values (Petroliagis et al. 2011; Gisinger et al. 2013). To obtain hourly data, horizontal wind fields are taken from ECMWF analyses at 0000 and 1200 UTC and, for the remaining times, from the short-term forecasts in the range from +1 to +11 h [the time availability of data is in Maass (2015)]. At such a very short range, the forecasts are nearly indistinguishable from the analyses, and therefore they can be used as realistic surrogates at the times at which the latter are missing (also, we did not consider the analyses at 0600 and 1800 UTC, but we did consider the forecast at +6 h). Data cover a wide region extending from 30° to 75°N and from 25°W to 45°E, considering both onshore and offshore grid points over almost all of Europe, including Iceland on the west side.

In contrast with climatological studies, which cover longer time periods for which coarser reanalysis data with an unchanged model formulation are normally used, here we exploit information from higher-resolution operational model outputs. This choice has several advantages. First, the higher-resolution fields (the horizontal grid spacing in the whole period analyzed in this study is ~16 km) make it possible to reproduce some meso-β-scale features that otherwise could not be identified. This is especially important in areas like the Mediterranean where the rough orography combined with the complex morphology of the coastline can locally modulate the flow to strongly affect the wind regimes at meso-β and meso-γ scales (e.g., Mazón and Pino 2013b; Comin et al. 2015). The horizontal resolution of the ECMWF operational data also permits a meaningful comparison of onshore and offshore wind energy potential, at least far from the coastlines where the grid cells may contain both land and sea subregions. Last, during the 3-yr period (2012–14) that is considered here, the changes in the ECMWF modeling and data assimilation system were relatively minor and did not affect the 100-m wind field.

To compute the normalized energy potential (or capacity factor), wind fields are transformed into electricity-generation data in agreement with the output function for the specific turbine design. This value, which represents how much energy such a system would have actually generated (kW h) in each grid cell, is finally normalized by the potential capacity (kW), that is, the maximum energy extraction rate (3075 kW for the chosen turbine). The maximum annual energy generation is 3075 kW × 8760 h,[1] and so the maximum annual normalized energy potential is 8760 kW h kW^{-1}.

Some technical details on the wind generator must be assumed to evaluate the share of the overall kinetic energy that can be transformed into electricity. To this aim, a power curve that is representative of a typical wind turbine is assumed (Fig. 2, solid blue line): in this case, the Vestas Wind Systems A/S V112-3.0 MW Power Curve, in noise mode 0, is used, supposing a fixed air density of 1.225 kg m^{-3} (Vestas 2011). The output function (expressed in kilowatts) shows that no energy can be extracted for wind speeds that are lower than 3 m s^{-1} and higher than 25 m s^{-1} and that the asymptotic value of 3075 kW is reached at 13 m s^{-1}. Also, because of the nonlinear shape, the variability in wind speed can have a pronounced impact in the steepest part of the power curve. Notice also that reference power curves such as the one used in this study provide an ideal
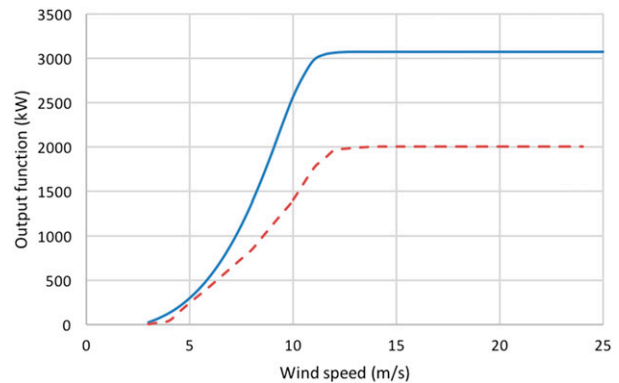

FIG. 2. Output function (kW) vs wind speed (m s^{-1}) for Vestas V112–3.0 MW (blue solid line). Also shown is the curve for the older Vestas V90-2.0 MW wind turbine (red dashed line).

quantitative relation between wind speed and power generation. Several meteorological parameters are known to have an impact on the actual power curve [see Eichhorn (2013) and the references therein]. Nevertheless, in this study such an impact is not considered and the results refer to the ideal case of the blue curve shown in Fig. 2.

One should consider that the ECMWF data, with a grid spacing of approximately 16 km, are representative of the wind regime in a limited area. In looking at the individual hourly maps by eye, it appears that the analysis is able to capture well not only the synoptic and meso-α scales, but also smaller (meso-β scale) features. Local differences in terrain and surface roughness may induce variability and determine substantial differences within a scale of some hundreds of meters, however—in particular, close to the coast or in complex terrain (Widén et al. 2015).

To exemplify the variety of scales that are present in a single map, Fig. 3 shows the 100-m wind speed at 0000 UTC 16 July 2012. Together with the intense flow associated with an extratropical cyclone centered north of Norway, a number of meso-β-scale high–wind speed stripes can be identified around or in the Mediterranean, extending westward of Gibraltar (levante wind; Scorer 1952) and eastward across the Strait of Bonifacio (between Sardinia and Corsica; Jiang et al. 2003), the Strait of Messina (northeast of Sicily; Bocciolone et al. 1993), and Calabria (the southernmost peninsular region in Italy; Federico et al. 2010). These intense low-level jets are due to the channeling of the flow across narrow straits or are associated, as in the latter case, with gaps in the orography. The topography responsible for these features generally extends horizontally for just a few tens of kilometers and vertically for some hundreds of meters above the ground; therefore one could not expect a priori that analysis fields at 100-m height with a
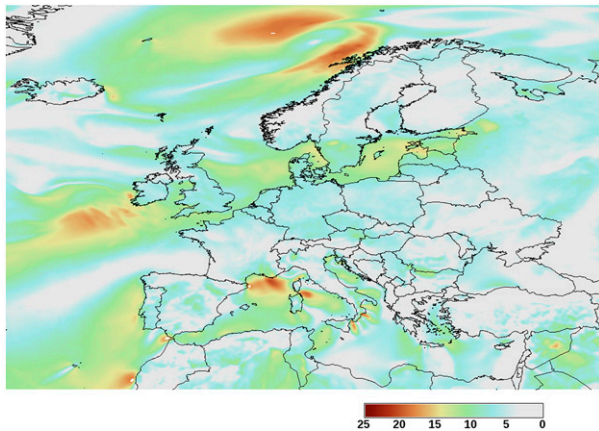
---

[1] 8784 kW h for leap years.

FIG. 3. The 100-m wind speed ($m s^{-1}$) at 0000 UTC 16 Jul 2012. The values above $13 m s^{-1}$ are shown in yellowish-reddish color to highlight the plateau in the power curve in Fig. 2; the values below $4 m s^{-1}$ are in white to identify the wind speeds from which almost no energy can be extracted.

FIG. 4. Sum of normalized wind energy ($kW h kW^{-1}$), averaged over all three years. The color scale nearly obscures the changes at the lower end of the range to highlight the regions with higher energy potential.

grid spacing of 16 km could capture these shallow structures with limited horizontal extent. In addition to channeling flows, other hourly maps identify the presence of downslope winds (bora wind and foehn); sea-breeze systems can also be identified, as discussed in section 5.

b. Irradiance data

The ECMWF also provides data for solar irradiance and cloud parameters. To derive optimized, site-specific, hourly data, different approaches to refining the ECMWF global model irradiance data have been investigated in the past, but with considerable limitations (Lorenz et al. 2009). Boilley and Wald (2015) showed the deficiencies of re-analysis data in comparison with satellite-based data, since the former tend to have a larger number of clear-sky days than are observed.

The solar radiation data used for this study are extracted from the satellite data retrieval scheme of the Satellite Application Facility on Climate Monitoring (CM SAF). Extensive validation has been performed in the last few years by using independent datasets (Posselt et al. 2011; Huld et al. 2012). The Mesoscale Atmospheric Global Irradiance Code (MAGIC) model (Mueller et al. 2009) generates the clear-sky irradiance, and cloud coverage is obtained from the Meteosat Second Generation data; from these two pieces of information, the solar ir-radiance can be derived. The time resolution of the data is 1 h for the region covered by Meteosat, with a spatial resolution that is a little coarser than 3 km at nadir. The analyzed domain includes a region extending from 30° to 60°N and from 15°W to 45°E; thus it is more limited to the west and north sides as compared with the wind data.
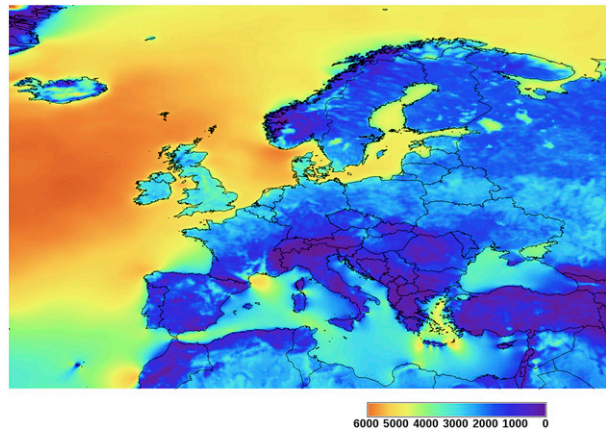
The data are available on request from CM SAF (http://www.cmsaf.eu). In the user interface, the global and direct irradiance components are named surface incoming shortwave (SIS) and surface incoming direct (SID). By default, these data are available only as daily averages. On request, the instantaneous data can also be made available.

3. Wind energy potential

The wind data at 100-m height are analyzed to cal-culate the wind energy potential. The yearly averaged integrated wind energy, calculated as explained in sec-tion 2a over the whole dataset of three years, is shown in Fig. 4. The highest potential is reached offshore in the region of the Atlantic Ocean delimited by Iceland on the north, the Iberian Peninsula on the south, and the British Isles and Norway on the east. This area is located between two semipermanent large-scale features: the Icelandic low and the Azores high. As a consequence, it is generally characterized by a large pressure gradient, associated with the transit of frontal systems moving eastward across the ocean along the Atlantic "storm track" (Hoskins and Hodges 2002).

Although the highest energy potential is present over the ocean at high latitudes, high values can also be identified in the southern part of the domain, near the Atlantic coasts of Morocco (the so-called chergui or sharqi wind) and in the Mediterranean Sea. The latter maxima are associated with intense and nearly per-sistent meso-α- and meso-β-scale patterns, like the etesians in the Aegean Sea (Koletsis et al. 2010) and the mistral blowing in the Gulf of Lyon (Jiang et al. 2003). Onshore, the maximum energy potential, which is much
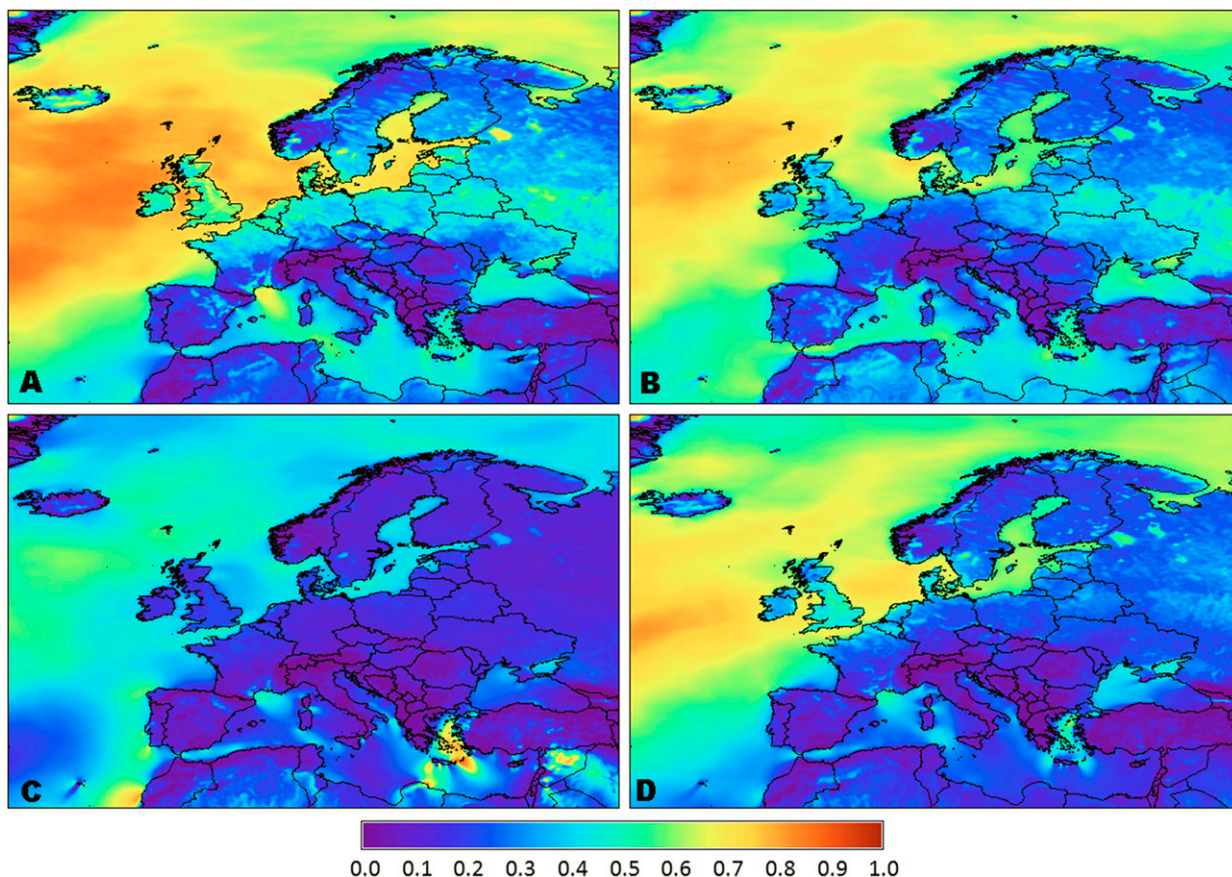
FIG. 5. Wind energy capacity factor, averaged over all three years, in (a) December, (b) March, (c) July, and (d) October. The maximum values achieved among the three years range from 0.90 to 0.92 kW h kW^{-1} in December, from 0.88 to 0.99 kW h kW^{-1} in July, and from 0.81 to 0.92 kW h kW^{-1} in October; the maximum value is constant at 0.88 kW h kW^{-1} in March. The minimum is 0 kW h kW^{-1} in all years. The thresholds in the color bar at 0.4 (from blue to cyan) and 0.7 (from yellow to orange)—with rapid changes within this range and more uniform shades outside this range—are chosen to highlight the regions with low and high capacity.

smaller than that over the sea, is over Iceland, the British Isles, and Denmark and is elongated along a narrow strip extending from west to east across central Europe. Areas with high energy potential can be also identified in the interior of northern Africa and the Middle East. Other local spots of high wind energy potential are present across the domain. Because of the coarse resolution, the role of the orography cannot be correctly detected, although it should significantly modulate the wind speed at local scale. As a consequence, minima occur over major mountains such as the Alps while, for instance, effects due to wind channeling in deep valleys are not visible at the given resolution.

From the perspective of determining whether an area can be considered to be favorable to wind energy production, it is important to determine not only its annual-average potential distribution but also how it changes on a monthly scale. Figure 5 shows the wind energy capacity factor in December, March, July, and October,

which is representative of the energy distribution in the four seasons. The capacity factor is the ratio of actual energy output to the output if the wind turbines produced at their nominal power at all times. The theoretical maximum is therefore equal to 1 kW h kW^{-1}.

A strong variation is apparent. In December, the maximum values (up to 0.86)[2] are observed over the Atlantic Ocean and the North and Baltic Seas. At lower latitudes, high potential (higher than 0.6) is present in the northwestern Mediterranean, associated with the mistral, which is persistent throughout the winter season, extending partially inland along the Garonne and Rhone Valleys (identified by the two relative maxima in southern France). Some meso-β-scale features, such as the outflow across the Ebro Valley in Spain (Mazón and Pino 2013a) and the bora wind in the northern Adriatic

---

[2] For brevity, we will omit the units in the following discussion.

(Ricchi et al. 2016), are present as well. Inland, a band of high potential extends longitudinally from the British Isles and northern France to eastern Europe, reflecting the climatological circulation patterns in winter (e.g., according to the ERA-40; Kållberg et al. 2005).

In July, the wind energy potential distribution changes dramatically. The maximum capacity factor (0.88), which is even higher than in December, is observed at much lower latitudes, near the Atlantic coast of Morocco (chergui wind); in the Aegean Sea (Etesian winds), where the wind speed is locally enhanced by the interaction with the peninsular part of Greece, the Cyclades, and Crete (Miglietta et al. 2013); and in Syria (Al-Mohamad and Karmeh 2003). Some local channeling flows are also apparent in the Mediterranean. An area of relative minimum is positioned in the Atlantic, in front of the Iberian Peninsula, and corresponds to the average location of the Azores high in summer (Kållberg et al. 2005). As expected, in March and October the energy distribution has some similarities with the December and July maps, although with a weaker general intensity. In particular, the patterns in March are more similar to those in December, whereas the October distribution is remarkably similar to the July map in the Mediterranean Basin.

The top panel of Fig. 6 shows how the monthly mean of the wind capacity factor, averaged over the whole domain, changes during the year.[3] The values range from 0.28 in July to 0.48 in December, with a yearly average of 0.38. The monthly fluctuations may be locally reversed; for example, Fig. 5 shows that in the Aegean Sea the potential is much higher in summer than in winter. In considering separately the land grid points (Fig. 6, middle panel) and the sea grid points (Fig. 6, bottom panel) a similar monthly variation is observed, although over a different range of values: offshore, the average capacity factor is much higher (0.51), with a monthly peak of 0.61 in December and February; inland, the yearly average falls to 0.21, which is close to the actual capacity factor for European wind turbines (Boccard 2009; Vitina et al. 2015),[4] and the value is very low in particular in July and August (0.14).

In contrast, the effect of time of day on the normalized hourly wind potential is small, at least on a continental domain, as in Drechsel et al. (2012); considering only the principal synoptic hours, the potential ranges from 0.38
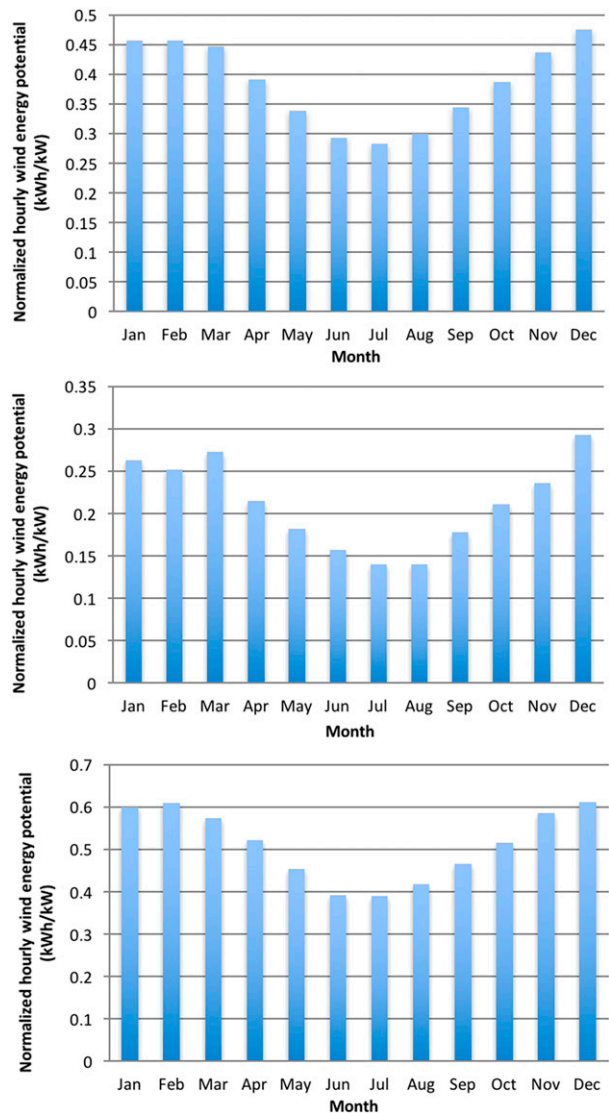

FIG. 6. Monthly-averaged normalized hourly wind energy potential (kW h kW^{-1}), averaged over 3 yr, (top) over the whole domain, (middle) over the onshore-only grid cells, and (bottom) over the offshore-only grid cells.

at 0600 UTC to 0.39 at 1800 UTC. Appreciable variations can, however, be locally identified when, instead of considering the whole continental domain, limited regions affected by circulations with diurnal evolution (e.g., sea and land breeze) are analyzed. If one used a ''local solar time'' time stamp rather than a ''UTC'' time stamp for each longitude column, greater variation could be distinguished over the whole domain, because diurnal cycles would be synchronous; this would be important especially in winter, when the daylight lengths are much shorter.

The standard deviation of the normalized hourly wind energy potential can be useful in providing some

---

[3] Averages are calculated as an arithmetic average of all grid cells in the given region.

[4] On the basis of data from the European Network of Transmission System Operators for Electricity (ENTSO-E) and British Petroleum, the capacity factor for wind power in Europe in 2015 was about 23.7% (see http://power.bghot.com).

indication on the variability of wind patterns. The fluctuations over the year of its monthly average (not shown) are similar to that shown in the top panel of Fig. 6, with values ranging from a minimum of 0.16 in June to a maximum of 0.23 in November and December. In contrast with the results inland and for the whole domain, however, offshore the maximum domain-averaged standard deviation occurs in autumn, with a peak in October. This result corresponds to a larger variability of synoptic circulation patterns, which are mainly responsible for the wind regime over the ocean, in that period of the year.

4. Solar energy potential

As discussed in section 2, solar radiation data from CM SAF have been extensively validated, showing an overall mean bias error (MBE) of less than 2% and a standard deviation of individual point MBE of ~5% (Posselt et al. 2011; Huld et al. 2012). Given also that their horizontal resolution is 3 km, which is much finer than that of the wind field, data from CM SAF may be considered to be accurate enough for the purposes of this study.

The energy output of PV systems depends on a number of factors apart from the solar radiation. In particular, the module efficiency depends also on the module temperature. The model used to include this effect has been taken from Huld et al. (2011), in which reference the model coefficients used for crystalline silicon PV modules can also be found. The module temperature in turn depends on the ambient air temperature, irradiance, and wind speed, modeled using the model of Faiman (2008), with coefficients for crystalline silicon modules taken from Koehl et al. (2011). For more details about the calculations, see Huld and Gracia Amillo (2015). In that study, the effects of spectral variations have also been considered and were found to be small for crystalline silicon in Europe. For this reason, spectral effects have not been considered in this study. Because the description of the PV performance models is spread over several references, we have included a brief summary in the appendix.

For the PV power simulation, the solar radiation data are hourly values as described above. The 10-m wind speed and 2-m air temperature fields are taken from the ECMWF operational forecasts. These data have a temporal resolution of 3 h, linearly interpolated to hourly values. PV modules are generally mounted close to the ground: for this reason, the 10-m wind speed has been rescaled to 2 m above ground.

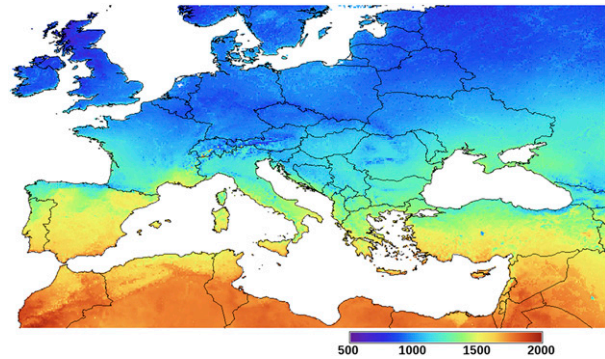Figure 7 shows the PV yearly energy potential, averaged over the 3-yr period analyzed here. The values are

FIG. 7. The PV yearly energy potential (10^2 kW h kW^{-1} yr^{-1}).

scaled to include system losses, which make no difference to the correlation analysis since they are represented by a constant factor. Because of the higher resolution when compared with wind data, the effect of the mountains is more evident, with a reduction in PV potential along the orography. Together with the latitude dependence, which reflects the different apparent solar height above the horizon, significant changes are also present among points at the same latitude. For example, in the Mediterranean, the northeastern part of Spain has much more PV energy potential than do northern Italy and the Balkan Peninsula, although all of these regions are at the same latitude.

Such a difference can be explained by considering the different average MSLP configuration in these regions. As shown in Fig. 1a, on average the Azores high affects the Iberian Peninsula while a wide cyclonic circulation affects the central Mediterranean. The climatological cloud cover reflects the differences in large-scale pressure patterns (Meerkötter et al. 2004a,b).

To represent how the PV potential changes during the year, Fig. 8 shows the monthly average of the capacity factor in December, March, July, and October. The monthly distribution is similar to the yearly average (Fig. 7): the large-scale patterns that are responsible for the longitudinal gradient of PV potential apparently persist throughout the year. The monthly variation is larger at high latitudes and is smaller in the southern Mediterranean. Figure 8 shows also that the intermonthly variations reflect the cycle of solar radiation: the capacity factor averaged over the domain ranges from a minimum in winter (the lowest value of the capacity factor is 0.072 in December) to a maximum from May to August (the peak capacity factor of 0.241 is in July). Conversely, the standard deviation of the hourly data (not shown) reaches a maximum in December and a minimum in July in reflection of the presence of more stable conditions in summer.
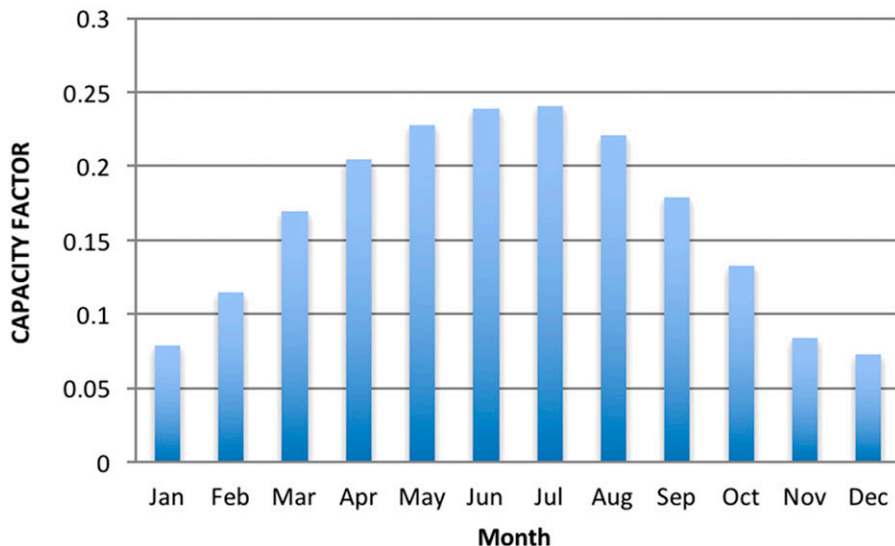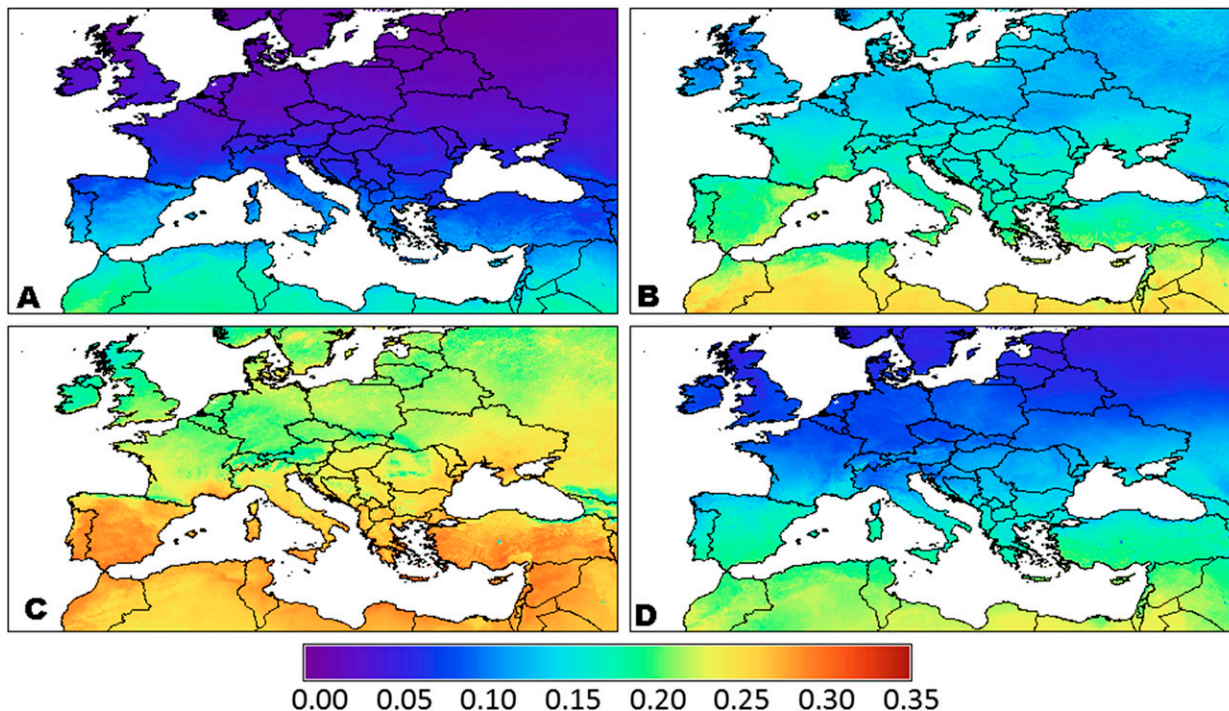
FIG. 8. PV energy potential, shown as the average monthly capacity factor, for (a) December, (b) March, (c) July, and (d) October. The maximum (minimum) values achieved among the three years range from 0.21 to 0.22 (from 0 to 0.006) in December, from 0.28 to 0.29 (from 0.05 to 0.06) in March, from 0.32 to 0.34 (from 0.10 to 0.13) in July, and from 0.23 to 0.26 (from 0.025 to 0.03) in October. Also shown (bottom) are the monthly values averaged over the domain (30°–60°N, 15°W–45°E).

The annual solar irradiation and, hence, the PV energy yield will vary from year to year. A recent study (Huld and Trentmann 2015) calculated the variability of the annual totals of global horizontal solar irradiation from 31 yr of satellite-based solar radiation data. The results show that the annual solar irradiation varies with a standard deviation of 2%–3% in southern Europe. This rises to 4%–6% in most of central and northern Europe, with values slightly higher only in a few areas, such as the Scandinavian mountains.

In our limited dataset extending over three years, the interannual change appears to be significant in a limited area separating the Mediterranean countries from central Europe: in particular, southern France, northern

Italy, the Balkans, and southeastern Europe received significantly less irradiation in 2013 than in 2012. This can be, to a first approximation, explained in terms of the North Atlantic Oscillation (NAO) index. The normalized NAO in winter (December–March) 2012/13 was −2, whereas in winter 2011/12 (and in winter 2013/14) it was positive, at approximately +3 (Hurrell and National Center for Atmospheric Research Staff 2016). Positive (negative) values of the NAO index are also associated with stronger-than-average (weaker than average) westerlies over the midlatitudes, more intense weather systems, and wetter weather over northern (southern) Europe. This suggests that the track of the frontal systems across Europe shifted to lower latitudes in winter 2012/13, producing more persistent cloud coverage and reducing irradiation in southern Europe with respect to winter 2011/12. The strong signature of the NAO on renewable energy resources is consistent with the results of Jerez et al. (2013b) for southwestern Europe and Pozo-Vázquez et al. (2004) for the European Atlantic region.

5. Complementarity of wind and PV energy sources

A comparison of Fig. 6 with Fig. 8 reveals an apparent complementarity of wind and solar resources, showing that the two distributions are out of phase on monthly basis. In the following, the correlation coefficients are calculated in a pointwise fashion, with the field with higher resolution (solar radiation) being sampled at the grid points given by the wind field. An analysis of the complementarity among different locations is not considered here. It is clear that solar and wind energy production should be as complementary as possible to assure smooth and efficient electricity generation. Such a property has been analyzed from different perspectives; for example, in the Iberian Peninsula (Jerez et al. 2013a,b), Italy (Monforti et al. 2014), Brazil (dos Anjos et al. 2015), Britain (Bett and Thornton 2016), Serbia (Gburčik et al. 2013), southern Australia (Mosadeghy et al. 2016), China (Liu et al. 2013), and Canada (Hoicka and Rowlands 2011).

For the calculation of correlation, we consider hourly data, daily averages, and monthly averages to assess the local complementarity at different time scales. The wind–solar correlation coefficients are calculated at the points of coordinates (x, y). Since the solar radiation and the wind speed data have different spatial resolution, the solar radiation data are sampled at the grid points determined by the wind data, with no spatial averaging of the solar data. Given the time series of wind $W_h(x, y, t)$ and PV potential $S_h(x, y, t)$ calculated at the hours $t = 1$,

N_{tot} (where $N_{tot} = 26\,304$ is the total number of hours contained in the three analyzed years), the correlation coefficient for the hourly data is provided by

$$R_h(x, y) = \frac{\sigma_{h,WS}}{[(\sigma_{h,W})(\sigma_{h,S})]^{1/2}}, \tag{1}$$

with

$$\sigma_{h,WS} = \sum_{t=1}^{N_{tot}} \{[W_h(x, y, t) - W(x, y)][S_h(x, y, t) - S(x, y)]\}, \tag{2}$$

$$\sigma_{h,W} = \sum_{t=1}^{N_{tot}} [W_h(x, y, t) - W(x, y)]^2, \quad \text{and} \tag{3}$$

$$\sigma_{h,S} = \sum_{t=1}^{N_{tot}} [S_h(x, y, t) - S(x, y)]^2, \tag{4}$$

where $W(x, y)$ and $S(x, y)$ are the 3-yr averages of the hourly wind and solar potential, respectively. The correlation coefficients for daily (R_d) and monthly (R_m) energy potential can be calculated similarly, but the time series of daily-averaged (for $t = 1, 1096$) and monthly-averaged (for $t = 1, 36$) wind and PV energy potential and their averages are used instead of the hourly values.

Note that, although the above description is given in terms of spatial points (x, y), the wind speed and solar radiation data are aggregates over areas covering the size of the spatial resolution of the respective datasets. Therefore, the correlation calculated between wind power and solar power should be considered to be the correlation between the combined wind and solar power output of a representative selection of wind turbines and PV systems within each spatial cell in the domain common to the two datasets.

For the hourly correlation R_h, the inclusion in Eq. (1) of nighttime data, during which time the irradiation is constantly zero, should be properly interpreted. From the point of view of the optimization of energy resources, including nighttime values is meaningful only when the wind speed is large enough to compensate for the absence of PV production. Only in this eventuality will negative values of correlation correspond to an effective complementarity of the resources and to a possible reduction in energy storage. From the mathematical definition of correlation, the inclusion of nighttime values in Eq. (1) has two effects relative to the case in which only daytime values are considered: it reduces $S(x, y)$ (e.g., for a day with equal duration of daytime and nighttime, the mean PV would be halved), and it contributes with negative terms $S_h(x, y)$ to the sum in Eq. (2). These factors can significantly modulate the intensity of the correlation. For example, for a region with a prevailing wind circulation having strong diurnal variability—for example, a sea
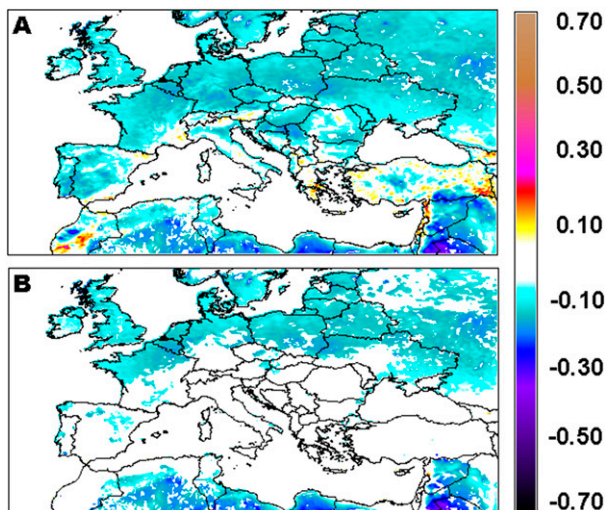
FIG. 9. Hourly correlation (a) over the whole 3-yr period and (b) over the same period but with the constraint that wind energy potential be higher than $2000\,kW\,h\,kW^{-1}\,yr^{-1}$. The regions with very high correlation (anticorrelation) are shown in brown (black), the regions with moderate-to-high correlation (anticorrelation) are colored from red to pink (from blue to purple), and those with weak correlation (anticorrelation) are colored in yellow (cyan) through white.

breeze (katabatic flows) with a maximum (minimum) value of $W_h(x, y)$ during daytime and a minimum (maximum) during nighttime—the correlation coefficient would be much more positive (negative) than including only daytime values.

Figure 9a shows the hourly local correlation over the three years that are considered here. Values are negative in most of the domain, suggesting a widespread possible local complementarity of renewable resources. Areas with positive correlation are mainly near the orography (Atlas, Alps, and Turkish mountains) and in the eastern part of the domain, in particular along the coast of Syria and Lebanon; negative values are present across central Europe, northern Africa, and the inland Middle East. The limited extent of areas of positive correlation, associated with specific circulation patterns (e.g., foehn), was noted for a similar study over Italy (Monforti et al. 2014).

To limit the investigation of complementarity to areas where the exploitation of renewable resources is actually economically feasible, Fig. 9b highlights only the regions with yearly wind energy potential above the threshold of $2000\,kW\,h$ produced per kilowatt of nominal capacity installed and with nonnegligible solar–wind hourly correlation [i.e., absolute values of $R_h(x, y)$ that are below 0.08 are in white]. The areas that respond to the criteria of significant wind productivity are mostly associated with negative correlation. These are mainly concentrated in two regions: one on the southern and eastern side of the Mediterranean and the other one along a narrow band extending from the British Isles to Russia across central and eastern Europe.

In addition, R_h has been calculated separately for each month. Figure 10 shows the results for December, March, July, and October: a significant variation occurs during the year, showing in particular that in many regions the absolute value of $R_h(x, y)$ increases with the solar radiation. For example, in December (Fig. 10a) the positive correlation is confined to a few very small
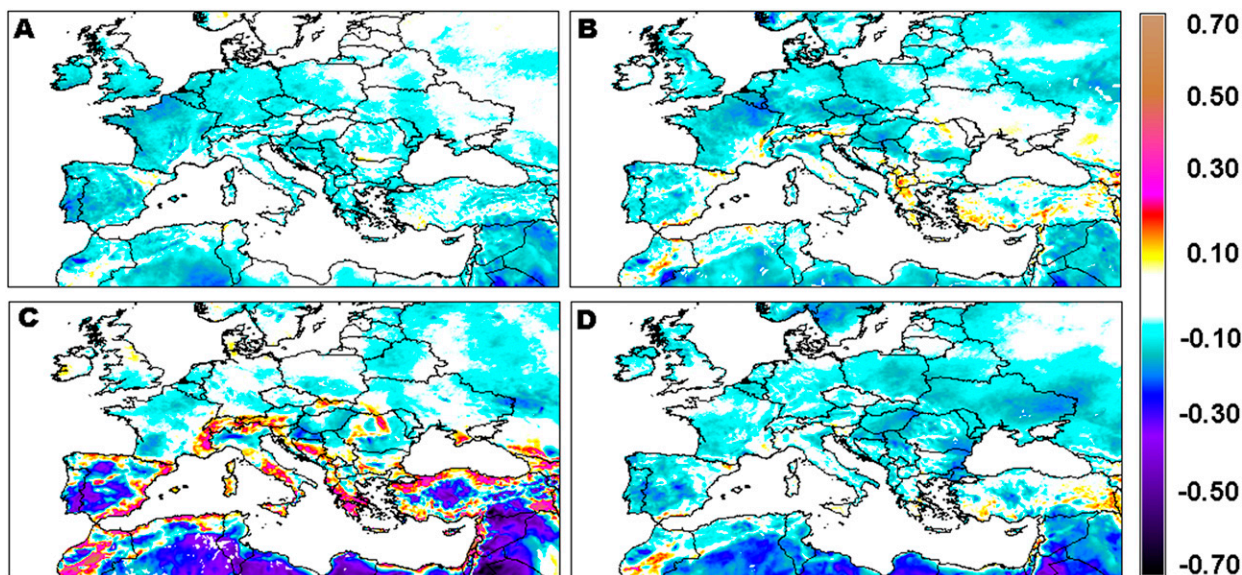

FIG. 10. Hourly correlation over the whole 3-yr period for (a) December, (b) March, (c) July, and (d) October.
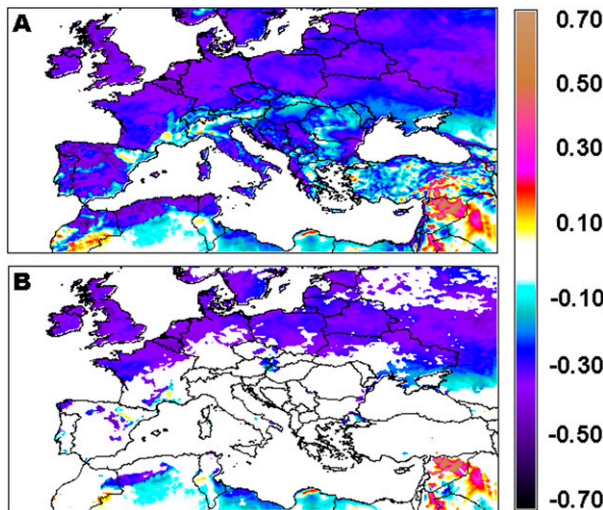
FIG. 11. As in Fig. 9, but for daily-averaged data.

FIG. 12. Wind energy capacity factor average for July at (a) 0000 and (b) 1200 UTC.

regions while a diffuse but relatively weak anti-correlation (minimum of R_h equal to -0.29) is widespread across Europe. In contrast, in July (Fig. 10c) large areas of positive correlation are present, mainly concentrated near the mountains and along the coastlines and probably associated with a strong diurnal cycle—as discussed earlier—while a strong anticorrelation (down to -0.70) is present in the southern part of the domain. In March (Fig. 10b) and October (Fig. 10d) the values of correlation are intermediate between December and July, with a prevailing presence of regions with weak anticorrelation.

The local correlation for daily-averaged data R_d is shown in Fig. 11. In general, on a daily scale the correlation should be less influenced by the daily cycle. In comparing Fig. 11 with Fig. 9, which is relative to the hourly correlation R_h, differences are apparent: a stronger anticorrelation prevails, with values of R_d of less than -0.20 in most of the domain, while only a few regions show a positive local correlation. Differences are relevant in particular in northern Africa and along the coasts of Syria and Lebanon, where R_d has the opposite sign of R_h, as it is negative near the coast and positive inland. As shown in Fig. 11b, these inland regions have wind energy potential that is higher than $2000 \, \mathrm{kW \, h \, kW^{-1} \, yr^{-1}}$.

The peculiar response in the southeastern part of the domain requires a deeper investigation. As discussed above, a strongly positive (negative) hourly correlation can be indicative of a strong diurnal cycle, associated with a maximum wind during the day (night). Figure 12, showing the wind energy potential at 0000 and 1200 UTC in July, reinforces this idea: apparently, near the southeastern border of the domain, the wind potential
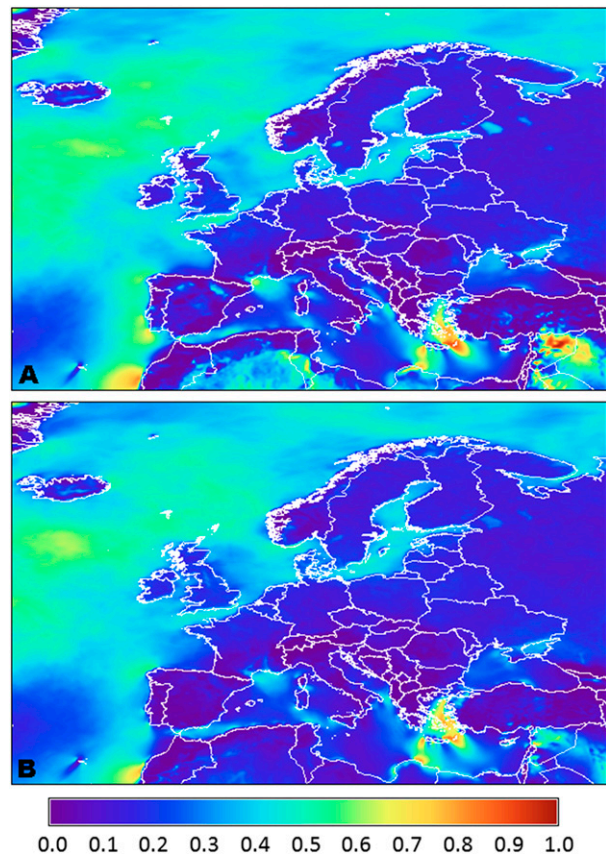
inland is stronger during the night and weaker during the day, which is opposite to what occurs near the coast, affected by sea-breeze circulation. Thus the abrupt change in correlation sign can be indicative of different circulations, with opposite daily cycles, in nearby regions. The interpretation in terms of R_d is less straightforward, considering that averages smooth out diurnal and monthly fluctuations.

The distribution of R_d in July and December (Fig. 13) is consistent with expectations, with extensive regions of positive correlation in summer, especially in the southern part of the domain where intense and persistent sea-breeze systems are present. In December, in contrast with R_h (Fig. 10a), extensive regions of positive daily correlation are also present across the domain. Such differences clearly address the need to focus on the time range in which one is interested before planning a strategy that is based on the complementarity of wind and solar resources.

The solar–wind complementarity on the basis of monthly-averaged data, which reflects the effect of the seasonality, is shown in Fig. 14. The pattern of R_m is
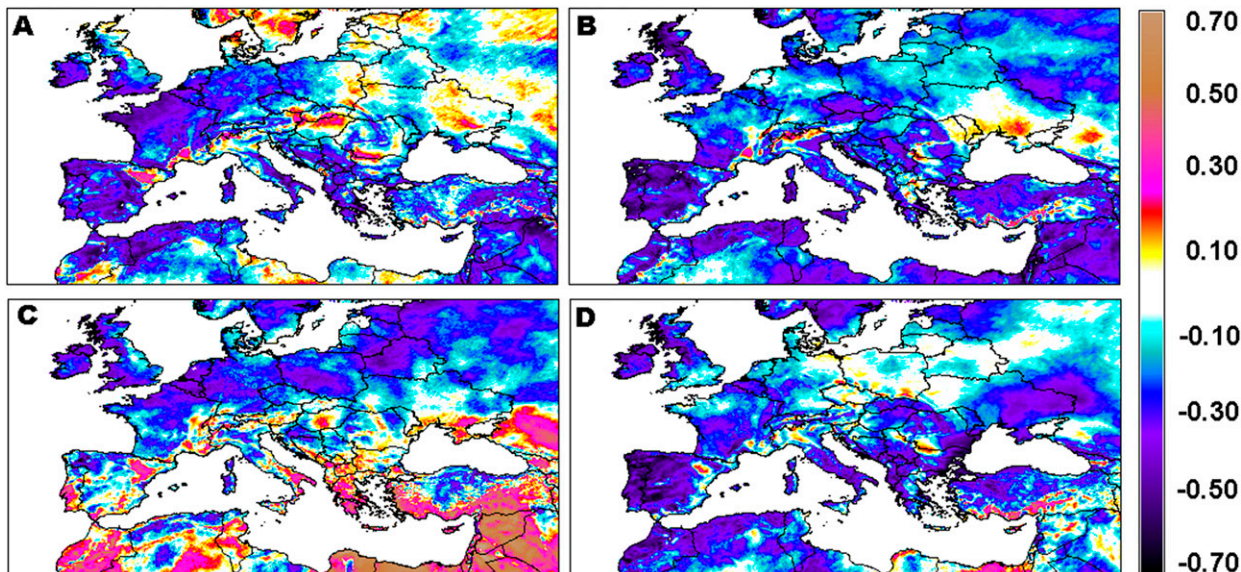
FIG. 13. As in Fig. 10, but for daily values.

similar to that shown for R_d in Fig. 11a but with a very large (in absolute value) correlation in extensive regions. The increase in absolute value with the extension of the time window that is considered for the correlation is consistent with previous results (Widén 2011; Monforti et al. 2014) and is, in most of the domain, an indication of windy winters alternated with calm summers.

Figure 15 summarizes the variations of R_h and R_d averaged over the domain in the different months. The monthly variation is smooth from winter to summer months, and a steeper jump is observed from August to September. As shown in the previous figures, R_h is generally less negative than R_d, with averages of -0.07 and -0.15, respectively. In particular, the monthly fluctuations in R_h appear to be limited, ranging from approximately -0.04 in June to -0.09 in September and October. For R_d, the weakest anticorrelation is in July (-0.06) and the minimum value is reached in March

(-0.23), with a secondary peak in October. In fact, as shown in Figs. 13b–d, the latter two months are characterized by a limited extent of areas with positive correlation, mainly confined to near the mountains and eastern Europe, whereas the anticorrelation is dominant in most of the continent, reaching its maximum on the west coasts of the Iberian Peninsula, Scotland, and Norway (and on the eastern Mediterranean coast). The average monthly MSLP maps (not shown) suggest that the largest anticorrelation corresponds to areas characterized by calm and sunny days (e.g., the Iberian Peninsula under the direct effect of the Azores high) or by windy and cloudy days (in the areas of strong pressure gradient, directly exposed to the Atlantic frontal systems on the western coasts of Scotland and Norway).
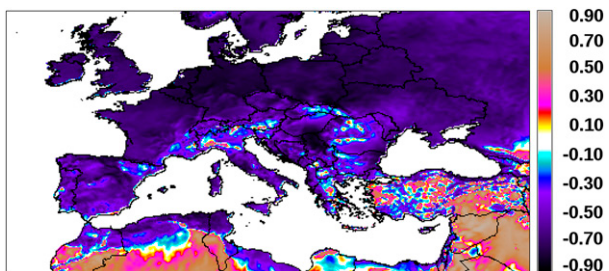

FIG. 14. As in Fig. 9a, but for monthly values. Note that the color scale extends further than in the previous figures.
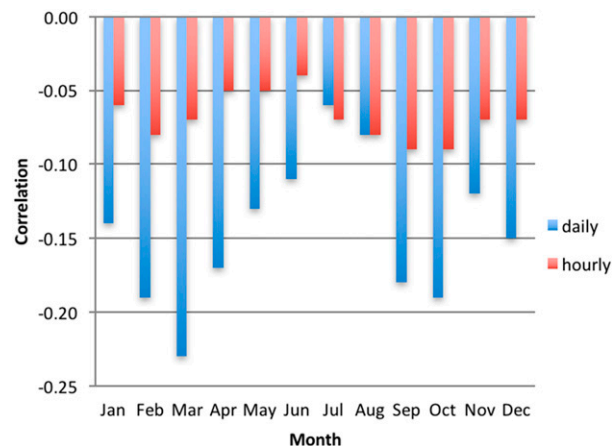

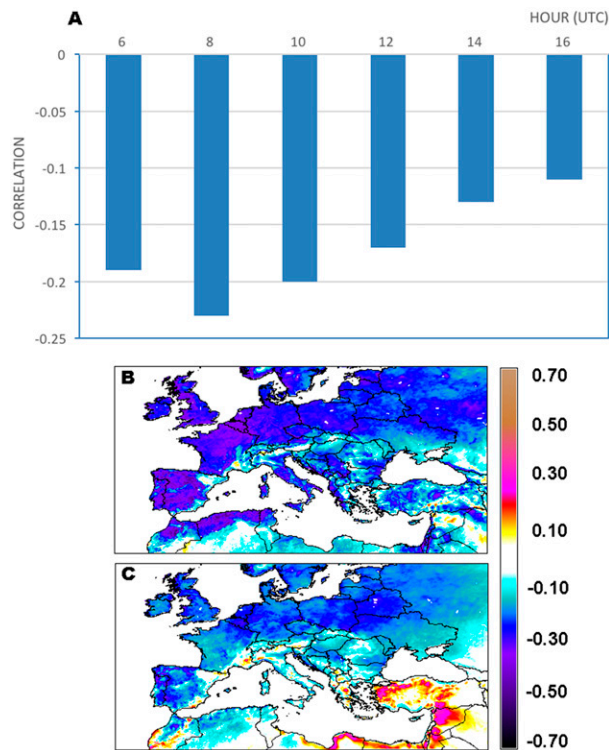FIG. 15. Monthly variation of R_h and R_d.

FIG. 16. (a) Variation of R_h with hour (UTC) and hourly correlation maps at (b) 1000 and (c) 1600 UTC.

Figures 10 and 13 have shown that the variations during the year can be very different depending on the region, for both hourly and daily data. Therefore, it is important to see how the monthly fluctuations change among different subregions, suggesting different strategies of energy storage depending on the area. This is left for future studies. Here, we note only that locally the hourly correlation averaged during the three years can be as low as −0.36 and that the average during summer months can reach −0.71. This confirms that the complementarity of the two renewable sources can be locally important and economically feasible.

Last we consider the variation of the domain-averaged correlation with time, which is also essential information for the energy community, taking into account the diurnal variability of demand. Analyzing the data for different hours (including only the period from 0600 to 1600 UTC, when most regions receive solar radiation during most of the year),[5] we see that the anticorrelation prevails at all times, being at a maximum in the morning (at 0800 UTC) and decreasing

quasi-linearly at later times (Fig. 16a). This is partly due to the extent of the regions with positive correlation, which is limited to small areas in the morning (Fig. 16b) but covers the south-southeastern coastlines of the Mediterranean Basin in the afternoon (Fig. 16c). This pattern can be attributed to the triggering and intensification of the sea-breeze circulation in the late morning and afternoon (windy and clear days; Figs. 8c and 12b), which is widespread along the southeastern Mediterranean coast during most of the year (not shown).

6. Conclusions

The analysis of data of wind and solar energy on different scales, both in time and space, is an important component for energy production. Indeed, the complementarity of the two sources can modulate the needs for energy storage in systems incorporating both sources. The highest complementarity should be searched for to assure continuous coverage and, at the same time, to avoid production that is higher than demand.

In this work, the local complementarity of wind and PV energy over Europe is analyzed at different time scales, studying the role of monthly variations and geographical effects over a 3-year period. In particular, we found the following:

- A strong monthly variation of wind potential in terms of location and intensity exists. The maximum averaged potential is offshore at northern latitudes, and in summer the peak is observed in the Mediterranean, associated with intense and nearly persistent mesoscale patterns. The ECMWF operational data used for the 100-m wind are appropriate to represent wind patterns at continental scale: they are able to identify synoptic-scale features, which determine the position of the frontal systems moving along the Atlantic Ocean, and meso-α-scale features; they cannot represent properly the flow over and around the orography at smaller meso-γ scales (Smith 1979; Miglietta and Buzzi 2001, 2004).
- There is a significant dependence of solar energy not only on latitude but also on longitude, associated with the presence of persistent large-scale pressure patterns; in contrast with wind data, irradiation data can properly represent the expected distribution near the mountains, having horizontal resolution of 3 km.
- An apparent complementarity of wind and solar resources on the annual time scale, since the two distributions are out of phase, was observed. Hourly data and daily- and monthly-averaged values are used to assess the local complementarity at different time scales. Correlation values are modulated by the month (higher absolute values in summer) and the considered

---

[5] The period of light time in northern Europe is limited to a few hours in winter, and therefore the correlation refers mainly to summer.

time period, with an increase in absolute value associated with the extent of the time window. A significant variation occurs during the year, with a diffuse anti-correlation widespread across Europe while large areas of positive local correlation are present, especially in summer near the mountains and along the coastlines, that are mainly associated with a strong diurnal cycle.

- The PV potential reaches its least variability when it is strongest, and wind power behaves in the opposite way. Thus, for both renewable sources, the minimum variability is in summer, suggesting that in that season the interannual variation is more limited and that the local complementarity changes less from year to year.

The extent of the 3-yr period analyzed in this study depends on the limited availability of the 100-m ECMWF wind field. Such a period is small for assessing interyear variability; from our limited dataset, we can see that for PV potential the fluctuations are relatively small, whereas they are larger for wind energy (see also Fig. 2 in Gisinger et al. 2013). We think that such variations do not affect the generality of our conclusions.

A limitation of this work is the use of specific devices for energy production. To evaluate how this constraint may modify the results, the analysis was repeated by using an older type of wind turbine (Vestas V90 with a rated generation of 2000-kW; red dashed line in Fig. 2): the changes were limited to a few percent in winter months, and the results remained nearly invariant in summer. The limited difference in response is related to the similar functional dependence of the normalized output, in particular in the high wind range from which most of the energy is extracted. Nevertheless, the wide applicability of results is still limited by the fact that, in both cases, the possible influence of other meteorological parameters such as turbulence or wind shear on the efficient conversion of wind speed into power has not been investigated.

A more important factor of uncertainty is the representativeness of the ECMWF analysis for near-surface wind data: the difference with observations can be large, especially in the presence of circulations of meso-γ scale or smaller. Also, following von Bremen et al. (2006), the largest forecast error should be expected for intermediate wind power values, whereas for high and low wind power productions the error should be comparable: since wind power and error are uncorrelated, the range of high wind speed corresponds to the same wind nominal power (Fig. 2).

Two follow-up steps are planned to complete the work that was presented here:

1) The first involves evaluation of the possible complementarity for complex generation systems covering transnational areas for large-scale power production.

TABLE A1. Coefficients used for the PV performance model given in Eq. (A1).

Coef	Value
k_1	$-0.017\,24$
k_2	$-0.040\,47$
k_3	-0.0047
k_4	1.49×10^{-4}
k_5	1.47×10^{-4}
k_6	5.0×10^{-6}

In other terms, we plan to extend the assessment study from a single point analysis to analysis over an extensive domain.

2) The second is to simulate a generation system that is composed of both wind and solar installations at different points that are randomly distributed (using a Monte Carlo method) all over Europe. Such results will extend to a continental scale the results that were obtained for Italy by Monforti et al. (2014).

APPENDIX

PV Performance Model Overview

The instantaneous power output of PV modules depends on a number of factors apart from the impinging solar irradiance. Among the most important factors are the following:

- The reflectivity of the PV module surface depends on the angle at which the sunlight hits the module surface. The angle of incidence of the sunlight depends on the location and module inclination and varies with time. In this study, this angle is found by using the model of Martin and Ruiz (2001). Using this model, Huld and Gracia Amillo (2015) found that this effect contributes to a fairly constant loss of about 3% in Africa.
- The PV module efficiency depends on the module temperature and irradiance, generally decreasing with increasing temperature and decreasing irradiance.
- The PV module temperature in turn depends on the in-plane irradiance, air temperature, and wind speed.
- The efficiency depends on the solar spectrum, which in turn varies with time and location. Gracia Amillo et al. (2015)

found that for crystalline silicon this effect is small in most areas (this is the case in Africa), and this effect is not considered in our study.

The PV power as a function of temperature and irradiance is modeled using the model described in Huld et al. (2011). The power $P(G, T)$ is given as a semiempirical formula:

$$
\begin{aligned}
P(G', T') &= G'[P_{\text{STC},m} + k_1 \ln(G') + k_2 \ln(G')^2 + k_3 T' \\
&\quad + k_4 T' \ln(G') + k_5 T' \ln(G')^2 + k_6 T'^2],
\end{aligned} \tag{A1}
$$

where the normalized in-plane irradiance and module temperatures are given by $G' = G/G_{\text{STC}}$ and $T' = T_m/T_{\text{STC}}$. Here, $k_1, \ldots, k_6$ are coefficients that were obtained by fitting measured data to Eq. (A1). The values used for crystalline silicon modules are taken from Huld et al. (2011) and are listed in Table A1, rescaled to a nominal PV power of 1 W.

PV module temperature is estimated using the model proposed in Faiman (2008). The model expressed the module temperature T_{mod} as a function of the ambient temperature T_{amb}, in-plane irradiance G, and wind speed w:

$$
T_{\text{mod}} = T_{\text{amb}} + \frac{G}{U_0 + U_1 w}.
$$

The coefficients $U_0 = 26.9$ and $U_1 = 6.2$ have been taken from Koehl et al. (2011) as an average of several different results for crystalline silicon modules.

REFERENCES

Al-Mohamad, A., and H. Karmeh, 2003: Wind energy potential in Syria. *Renewable Energy*, **28**, 1039–1046, doi:10.1016/S0960-1481(02)00186-6.

Bett, P. E., and H. E. Thornton, 2016: The climatological relationships between wind and solar energy supply in Britain. *Renewable Energy*, **87**, 96–110, doi:10.1016/j.renene.2015.10.006.

Boccard, N., 2009: Capacity factor of wind power realized values vs. estimates. *Energy Policy*, **37**, 2679–2688, doi:10.1016/j.enpol.2009.02.046.

Bocciolone, M., M. Gasparetto, S. Lagomarsino, G. Piccardo, C. F. Ratto, and G. Solari, 1993: Statistical analysis of extreme wind speeds in the Straits of Messina. *J. Wind Eng. Ind. Aerodyn.*, **48**, 359–377, doi:10.1016/0167-6105(93)90146-F.

Boilley, A., and L. Wald, 2015: Comparison between meteorological re-analyses from ERA-Interim and MERRA and measurements of daily solar irradiation at surface. *Renewable Energy*, **75**, 135–143, doi:10.1016/j.renene.2014.09.042.

Coker, P., J. Barlow, T. Cockerill, and D. Shipworth, 2013: Measuring significant variability characteristics: An assessment of three UK renewables. *Renewable Energy*, **53**, 111–120, doi:10.1016/j.renene.2012.11.013.

Comin, A. N., M. M. Miglietta, U. Rizza, O. C. Acevedo, and G. A. Degrazia, 2015: Investigation of sea-breeze convergence in Salento Peninsula (southeastern Italy). *Atmos. Res.*, **160**, 68–79, doi:10.1016/j.atmosres.2015.03.010.

Dos Anjos, P. S., A. S. Alves da Silva, B. Stošić, and T. Stošić, 2015: Long-term correlations and cross-correlations in wind speed and solar radiation temporal series from Fernando de Noronha Island, Brazil. *Physica A*, **424**, 90–96, doi:10.1016/j.physa.2015.01.003.

Drechsel, S., G. J. Mayr, J. W. Messner, and R. Stauffer, 2012: Wind speeds at heights crucial for wind energy: Measurements and verification of forecasts. *J. Appl. Meteor. Climatol.*, **51**, 1602–1617, doi:10.1175/JAMC-D-11-0247.1.

Eichhorn, K., 2013: The change of power curves as a function of various meteorological parameters. M.S. thesis, Dept. of Geo- and Atmospheric Sciences, University of Innsbruck, 65 pp. [Available online at http://acinn.uibk.ac.at/sites/default/files/Masterarbeit_Eichhorn_Katharina_kleiner.pdf.]

Faiman, D., 2008: Assessing the outdoor operating temperature of photovoltaic modules. *Prog. Photovoltaics*, **16**, 307–315, doi:10.1002/pip.813.

Federico, S., L. Pasqualoni, L. De Leo, and C. Bellecci, 2010: A study of the breeze circulation during summer and fall 2008 in Calabria, Italy. *Atmos. Res.*, **97**, 1–13, doi:10.1016/j.atmosres.2010.02.009.

García-Bustamante, E., and Coauthors, 2013: Relationship between wind power production and North Atlantic atmospheric circulation over the northeastern Iberian Peninsula. *Climate Dyn.*, **40**, 935–949, doi:10.1007/s00382-012-1451-8.

Gburčik, V., S. Mastilović, and Ž. Vučinić, 2013: Assessment of solar and wind energy resources in Serbia. *J. Renewable Sustainable Energy*, **5**, 041822, doi:10.1063/1.4819504.

Gisinger, S., G. J. Mayr, J. W. Messner, and R. Stauffer, 2013: Spatial and temporal variation of wind power at hub height over Europe. *Nonlinear Processes Geophys.*, **20**, 305–310, doi:10.5194/npg-20-305-2013.

Gracia Amillo, A., T. Huld, P. Vourlioti, R. Müller, and M. Norton, 2015: Application of satellite-based spectrally resolved solar radiation data to PV performance studies. *Energies*, **8**, 3455–3488, doi:10.3390/en8053455.

Hoicka, C. E., and I. H. Rowlands, 2011: Solar and wind resource complementarity: Advancing options for renewable electricity integration in Ontario, Canada. *Renewable Energy*, **36**, 97–107, doi:10.1016/j.renene.2010.06.004.

Hoskins, B. J., and K. I. Hodges, 2002: New perspectives on the Northern Hemisphere winter storm tracks. *J. Atmos. Sci.*, **59**, 1041–1061, doi:10.1175/1520-0469(2002)059<1041:NPOTNH>2.0.CO;2.

Huld, T., and A. M. Gracia Amillo, 2015: Estimating PV module performance over large geographical regions: The role of irradiance, air temperature, wind speed and solar spectrum. *Energies*, **8**, 5159–5181, doi:10.3390/en8065159.

——, and J. Trentmann, 2015: Variability and trend in the annual solar irradiation determined from Meteosat satellite data. *Proc. 31st European Photovoltaic Solar Energy Conf. and Exhibition*, Hamburg, Germany, WIP Wirtschaft und Infrastruktur GmbH & Co. Planungs-KG, 2073–2076, doi:10.4229/EUPVSEC20152015-5BV.1.3.

——, G. Friesen, A. Skoczek, R. P. Kenny, T. Sample, M. Field, and E. D. Dunlop, 2011: A power-rating model for crystalline silicon PV modules. *Sol. Energy Mater. Sol. Cells*, **95**, 3359–3369, doi:10.1016/j.solmat.2011.07.026.

——, R. Müller, and A. Gambardella, 2012: A new solar radiation database for estimating PV performance in Europe

and Africa. *Sol. Energy*, **86**, 1803–1815, doi:10.1016/j.solener.2012.03.006.

Hurrell, J., and National Center for Atmospheric Research Staff, Eds., 2016: Hurrell North Atlantic Oscillation (NAO) index (station-based). UCAR/NCAR Climate Data Guide, accessed 26 May 2016. [Available online at https://climatedataguide.ucar.edu/climate-data/hurrell-north-atlantic-oscillation-nao-index-station-based.]

Jerez, S., R. M. Trigo, A. Sarsa, R. Lorente-Plazas, D. Pozo-Vázquez, and J. P. Montávez, 2013a: Spatio-temporal complementarity between solar and wind power in the Iberian Peninsula. *Energy Procedia*, **40**, 48–57, doi:10.1016/j.egypro.2013.08.007.

——, ——, S. M. Vicente-Serrano, D. Pozo-Vázquez, R. Lorente-Plazas, J. Lorenzo-Lacruz, F. Santos-Alamillos, and J. P. Montávez, 2013b: The impact of the North Atlantic Oscillation on renewable energy resources in southwestern Europe. *J. Appl. Meteor. Climatol.*, **52**, 2204–2225, doi:10.1175/JAMC-D-12-0257.1.

——, F. Thais, I. Tobin, M. Wild, A. Colette, P. Yiou, and R. Vautard, 2015: The CLIMIX model: A tool to create and evaluate spatially-resolved scenarios of photovoltaic and wind power development. *Renewable Sustainable Energy Rev.*, **42**, 1–15, doi:10.1016/j.rser.2014.09.041.

Jiang, Q., R. B. Smith, and J. Doyle, 2003: The nature of the mistral: Observations and modelling of two MAP events. *Quart. J. Roy. Meteor. Soc.*, **129**, 857–875, doi:10.1256/qj.02.21.

Kållberg, P., P. Berrisford, B. Hoskins, A. Simmons, S. Uppala, S. Lamy-Thépaut, and R. Hine, 2005: ERA-40 atlas. ECMWF ERA-40 Project Rep. 19, 191 pp. [Available online at http://www.ecmwf.int/sites/default/files/elibrary/2005/10596-era-40-atlas-note-large-pdf-file-683-mb-revised-version-posted-19012006.pdf.]

Koehl, M., M. Heck, S. Wiesmeier, and J. Wirth, 2011: Modeling of the nominal operating cell temperature based on outdoor weathering. *Sol. Energy Mater. Sol. Cells*, **95**, 1638–1646, doi:10.1016/j.solmat.2011.01.020.

Koletsis, I., K. Lagouvardos, V. Kotroni, and A. Bartzokas, 2010: The interaction of northern wind flow with the complex topography of Crete Island–Part 2: Numerical study. *Nat. Hazards Earth Syst. Sci.*, **10**, 1115–1127, doi:10.5194/nhess-10-1115-2010.

Liu, Y., L. Xiao, H. Wang, S. Dai, and Z. Qi, 2013: Analysis on the hourly spatiotemporal complementarities between China's solar and wind energy resources spreading in a wide area. *Sci. China Technol. Sci.*, **56**, 683–692, doi:10.1007/s11431-012-5105-1.

Lorenz, E., J. Hurka, D. Heinemann, and H. G. Beyer, 2009: Irradiance forecasting for the power prediction of grid-connected photovoltaic systems. *IEEE J. Sel. Top. Appl. Earth Obs. Remote Sens.*, **2**, 2–10, doi:10.1109/JSTARS.2009.2020300.

Maass, C., 2015: MARS content. European Centre for Medium-Range Weather Forecasts, accessed 26 May 2016. [Available online at https://software.ecmwf.int/wiki/display/UDOC/MARS+content.]

Martin, N., and J. M. Ruiz, 2001: Calculation of the PV modules angular losses under field conditions by means of an analytical model. *Sol. Energy Mater. Sol. Cells*, **70**, 25–38, doi:10.1016/S0927-0248(00)00408-6.

Mazón, J., and D. Pino, 2013a: Nocturnal offshore precipitation near the Mediterranean coast of the Iberian Peninsula. *Meteor. Atmos. Phys.*, **120**, 11–28, doi:10.1007/s00703-012-0229-1.

——, and ——, 2013b: The role of sea–land air thermal difference, shape of the coastline and sea surface temperature in the nocturnal offshore convection. *Tellus*, **65A**, 20 027, doi:10.3402/tellusa.v65i0.20027.

Meerkötter, R., G. Gesell, V. Grewe, C. König, S. Lohmann, and H. Mannstein, 2004a: A high resolution European cloud climatology from 15 years of NOAA/AVHRR data. *2004 Meteorological Satellite Conf.*, Prague, Czech Republic, European Organisation for the Exploitation of Meteorological Satellites, 542–550. [Available online at http://www.eumetsat.int/website/wcm/idc/idcplg?IdcService=GET_FILE&dDocName=PDF_CONF_P41_S5_MANNSTEIN_P&RevisionSelectionMethod=LatestReleased&Rendition=Web.]

——, C. König, P. Bissolli, G. Gesell, and H. Mannstein, 2004b: A 14-year European cloud climatology from NOAA/AVHRR data in comparison to surface observations. *Geophys. Res. Lett.*, **31**, L15103, doi:10.1029/2004GL020098.

Miglietta, M. M., and A. Buzzi, 2001: A numerical study of moist stratified flows over isolated topography. *Tellus*, **53A**, 481–499, doi:10.1111/j.1600-0870.2001.00481.x.

——, and ——, 2004: A numerical study of moist stratified flow regimes over isolated topography. *Quart. J. Roy. Meteor. Soc.*, **130**, 1749–1770, doi:10.1256/qj.02.225.

——, S. Zecchetto, and F. De Biasio, 2013: A comparison of WRF Model simulations with SAR wind data in two case studies of orographic lee waves over the eastern Mediterranean Sea. *Atmos. Res.*, **120–121**, 127–146, doi:10.1016/j.atmosres.2012.08.009.

Monforti, F., T. Huld, K. Bódis, L. Vitali, M. D'Isidoro, and R. Lacal-Arántegui, 2014: Assessing complementarity of wind and solar resources for energy production in Italy: A Monte Carlo approach. *Renewable Energy*, **63**, 576–586, doi:10.1016/j.renene.2013.10.028.

Mosadeghy, M., R. Yan, and T. K. Saha, 2016: Impact of PV penetration level on the capacity value of South Australian wind farms. *Renewable Energy*, **85**, 1135–1142, doi:10.1016/j.renene.2015.07.072.

Mueller, R. W., C. Matsoukas, A. Gratzki, H. D. Behr, and R. Hollmann, 2009: The CM-SAF operational scheme for the satellite based retrieval of solar surface irradiance—A LUT based eigenvector hybrid approach. *Remote Sens. Environ.*, **113**, 1012–1024, doi:10.1016/j.rse.2009.01.012.

Perez, R., and T. E. Hoff, 2013: Solar resource variability. *Solar Energy Forecasting and Resource Assessment*. J. Kleissl, Ed., Academic Press, 133–148.

Petroliagis, T., F. Pappenberger, and R. Buizza, 2011: Skill assessment of the new ECMWF 100-meter wind fields. *11th EMS Annual Meeting/10th European Conf. on Applications of Meteorology*, Berlin, Germany, European Meteorological Society, EMS2011-352. [Available online at http://presentations.copernicus.org/EMS2011-352_presentation.pdf.]

Posselt, R., R. Mueller, R. Stöckli, and J. Trentmann, 2011: Spatial and temporal homogeneity of solar surface irradiance across satellite generations. *Remote Sens.*, **3**, 1029–1046, doi:10.3390/rs3051029.

Pozo-Vázquez, D., J. Tovar-Pescador, S. R. Gámiz-Fortis, M. J. Esteban-Parra, and Y. Castro-Díez, 2004: NAO and solar radiation variability in the European North Atlantic region. *Geophys. Res. Lett.*, **31**, L05201, doi:10.1029/2003GL018502.

Ricchi, A., M. M. Miglietta, P. P. Falco, A. Benetazzo, D. Bonaldo, A. Bergamasco, M. Sclavo, and S. Carniel, 2016: On the use of a coupled ocean–atmosphere–wave model during an extreme cold air outbreak over the Adriatic Sea. *Atmos. Res.*, **172–173**, 48–65, doi:10.1016/j.atmosres.2015.12.023.

Santos-Alamillos, F. J., D. Pozo-Vázquez, J. A. Ruiz-Arias, V. Lara-Fanego, and J. Tovar-Pescador, 2012: Analysis of spatiotemporal balancing between wind and solar energy resources in the southern Iberian Peninsula. *J. Appl. Meteor. Climatol.*, **51**, 2005–2024, doi:10.1175/JAMC-D-11-0189.1.

Scorer, R. S., 1952: Mountain-gap winds; A study of the surface wind at Gibraltar. *Quart. J. Roy. Meteor. Soc.*, **78**, 53–61, doi:10.1002/qj.49707833507.

Smith, R. B., 1979: The influence of mountains on the atmosphere. *Advances in Geophysics*, Vol. 21, Academic Press, 87–230, doi:10.1016/S0065-2687(08)60262-9.

St. Martin, C. M., J. K. Lundquist, and M. A. Handschy, 2015: Variability of interconnected wind plants: Correlation length and its dependence on variability time scale. *Environ. Res. Lett.*, **10**, 044004, doi:10.1088/1748-9326/10/4/044004.

Vestas, 2011: General specification V112-3.0 MW 50/60 Hz. Vestas Wind Systems A/C Doc. 0011-9181 V05, 56 pp. [Available online at https://www.scribd.com/doc/225239542/Technische-Specificatie-Windturbine-Vestas-v-112-3-0-MW-5060-Hz.]

Vitina, A., and Coauthors, 2015: IEA Wind Task 26: Wind technology, cost, and performance trends in Denmark, Germany, Ireland, Norway, the European Union, and the United States: 2007–2012. IEA Wind Tech. Rep. NREL/TP-6A20-64332, 163 pp. [Available online at http://www.ieawind.org/index_page_postings/task26/IEA%20Wind%20Task%2026%20WP1%20Report%2064332.pdf.]

von Bremen, L., J. Tambke, N. Saleck, and D. Heinemann, 2006: Confidence in large-scale offshore wind farming: Wind power predictability and stable grid integration of 25 GW German wind power. *Sixth Int. Workshop on Large-Scale Integration of Wind Power and Transmission Networks for Offshore Wind Farms*, Delft, Netherlands, Energynautics GmbH, 277–284.

Widén, J., 2011: Correlations between large-scale solar and wind power in a future scenario for Sweden. *IEEE Trans. Sustainable Energy*, **2**, 177–184, doi:10.1109/TSTE.2010.2101620.

——, and Coauthors, 2015: Variability assessment and forecasting of renewables: A review for solar, wind, wave and tidal resources. *Renewable Sustainable Energy Rev.*, **44**, 356–375, doi:10.1016/j.rser.2014.12.019.